

High-performance quantum cascade lasers in the 7.3- to 7.8- μm wavelength band using strained active regions

Richard P. Leavitt
John L. Bradshaw
Kevin M. Lascola
Gregory P. Meissner
Frankie Micalizzi
Frederick J. Towner
John T. Pham

Maxion Technologies Inc.
5000 College Park Avenue, Suite 3121
College Park, Maryland 20740

Abstract. We consider the use of strained quantum cascade (QC) laser designs in the 7.3- to 7.8- μm wavelength region to improve the cw operating characteristics of these lasers at room temperature. We compare the performance of a QC laser with a strain-balanced active region with that of two similarly designed QC lasers with lattice-matched active-region layers, and we show that the strain-balanced design significantly outperforms the unstrained-layer designs in terms of threshold-current density, power slope efficiency, and cw output power at room temperature. A epi-side-down-mounted, double-channel ridge-geometry laser that was fabricated from the strained design with a ridge width of 13 μm and a cavity length of 3 mm produced cw output power in excess of 500 mW at room temperature. The characteristic temperature T_0 for the strained-layer design as determined from pulsed measurements between 25 and 80°C is 221.5 K, compared with a value of 194.0 K for one of the unstrained designs. © 2010 Society of Photo-Optical Instrumentation Engineers. [DOI: 10.1117/1.3498758]

Subject terms: quantum cascade lasers; semiconductor lasers; infrared lasers; strain balancing.

Paper 100275SSR received Apr. 1, 2010; revised manuscript received May 24, 2010; accepted for publication Jun. 1, 2010; published online Nov. 29, 2010.

1 Introduction

The demonstration of the first quantum cascade (QC) laser in 1994 (Ref. 1) and the subsequent realization of continuous-wave (cw), room-temperature operation of QC lasers in 2004 (Ref. 2) have enabled many civilian and military applications for these devices in the areas of chemical sensing, free-space communications, IR countermeasures, explosive detection, and industrial process control that had previously been considered impractical because of the lack of compact high-powered optical sources in the mid-IR spectral region. Since those seminal publications, efforts have been made to improve the performance of QC lasers at several different wavelengths, and stable single-mode operation has been achieved both by the use of external cavities³ and by fabricating distributed-feedback (DFB) lasers.⁴

The group at Northwestern University has demonstrated state-of-the-art performance of ridge-geometry QC lasers at wavelengths near 4.6 μm . Yu et al.⁵ demonstrated high performance of QC lasers with 4-mm cavity lengths, 10- μm ridge widths, and emission wavelengths of $\sim 4.6 \mu\text{m}$. For epi-up-mounted lasers with uncoated front facets and high-reflectance (HR) coated rear facets, an average output power of 633 mW in pulsed operation at 65% duty cycle and a cw output power of 469 mW were observed at room temperature. HR-coated lasers that were mounted epi-side down onto AlN submounts emitted 590 mW cw at room temperature. The Northwestern group also demonstrated⁶ single-facet cw output power as high as 1.25 W in an uncoated ridge QC laser mounted epi-down on a diamond heat sink, with a corresponding wall plug efficiency (WPE) of 12.5%, as well as 1.8 W of room-temperature, cw power and 11% WPE from a

laser fabricated from the same wafer with an HR-coated rear facet. In terms of output power, significant progress has also been made in the development of QC lasers with the buried-heterostructure (BH) geometry. A collaboration⁷ between researchers at Pranalytica and Harvard reported a 4.6- μm BH QC laser (5 mm cavity length, 11.6 μm ridge width, HR-coated rear facet) mounted epi-side down onto a diamond submount with a cw output power of 3 W at 293 K. The Northwestern group⁸ produced 2.6 W of cw output power with 17% WPE at room-temperature from a 4.6- μm BH QC laser (with a 5-mm cavity length, a 6.2- μm ridge width, and an HR-coated rear facet) mounted onto a diamond submount.

Unfortunately, the state of the art for longer wavelength QC lasers has not kept up with that of QC lasers at wavelengths below 6 μm , for which the best results have been achieved using strained-layer active-region designs. Even at 6 μm , to our knowledge the best result achieved to date produced 372 mW in a BH geometry,⁹ with a threshold current density J_{th} of 2.35 kA/cm^2 and a characteristic temperature $T_0 = 162 \text{ K}$. Longer wavelength lasers typically use unstrained designs; for example, Diehl et al.¹⁰ demonstrated a cw output power of 204 mW at 8.4 μm at room temperature in a BH laser, with $J_{\text{th}} = 1.39 \text{ kA}/\text{cm}^2$ and $T_0 = 162 \text{ K}$. Pflügl et al.¹¹ reported an uncoated BH laser at a wavelength of 9.5 μm that produced 180 mW per facet at 295 K, with $J_{\text{th}} = 1.54 \text{ kA}/\text{cm}^2$. At a wavelength of 8.8 μm , Yu et al.¹² demonstrated 294 mW of output power in a ridge laser operating cw at room temperature, with $J_{\text{th}} = 1.29 \text{ kA}/\text{cm}^2$ and a T_0 value of about 200 K. The only recent exception to this trend, to our knowledge, is a recent report from the Northwestern group¹³ of 620 mW being achieved in cw, room-temperature operation of a 10.2- μm -wavelength BH QC laser with a ridge width of 16.6 μm and a cavity length of 5 mm.

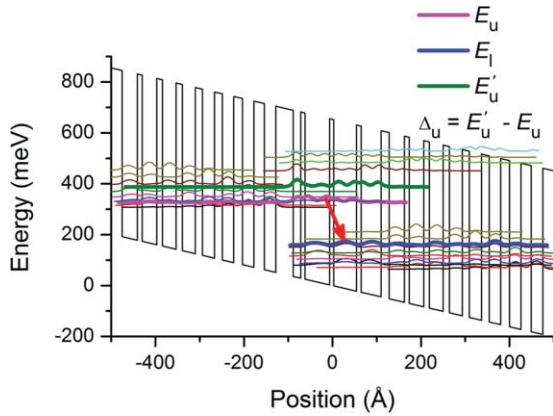


Fig. 1 Schematic energy-level/wave-function diagram for the strained QC laser design of wafer M738. Important active-section levels are indicated by thick lines. The optical transition is indicated by the red arrow. The light-green- and light-blue-colored levels near the upper right of the diagram are levels belonging to the excited injector miniband. The electric field is 40.4 kV/cm.

In this paper, we consider the use of strained QC laser designs in the 7.3- to 7.8- μm wavelength region. We compare the performance of a QC laser with a strain-balanced active region with that of two similarly designed QC lasers with lattice-matched active-region layers, and we show that the strain-balanced design significantly outperforms the unstrained-layer designs in terms of threshold-current density, power slope efficiency, and cw output power at room temperature. A epi-side-down-mounted, double-channel ridge-geometry laser that was fabricated from the strained design with a ridge width of 13 μm and a cavity length of 3 mm produced cw output power in excess of 500 mW at room temperature. The T_0 value for the strained design in pulsed operation is 221.5 K between 25 and 80°C, compared with 204.4 K for one of the unstrained designs over the same temperature range.

2 Design Considerations

For this work, we designed and grew a QC laser structure, wafer M738, with a strained active region. We also designed and grew two lasers, wafers M731 and M733, with unstrained active regions and with target wavelengths separated by $\sim 0.15 \mu\text{m}$. All three of the lasers were designed using a common quantum design algorithm (see the following).

Figure 1 shows a plot of the conduction band edge for a section of the active region of the strained design, M738, which consists of a single four-quantum-well active section with an eight-quantum-well injector section on either side of it, at an electric field of 40.4 kV/cm. Also shown in the figure are the moduli squared of the calculated wave functions for the bound and quasibound states supported by the structure, with the upper laser level (with energy E_u), the lower laser level (with energy E_l), and the active-section level lying immediately above the upper laser level in energy (with energy E'_u) indicated by bold lines. In this design, the well material is $\text{In}_{0.5734}\text{Ga}_{0.4266}\text{As}$ and the barrier material is $\text{In}_{0.4476}\text{Al}_{0.5524}\text{As}$; consequently, the conduction-band offset ΔE_c between barrier and well materials is 655 meV. In contrast, the unstrained designs use the lattice-matched

compositions $\text{In}_{0.5319}\text{Ga}_{0.4681}\text{As}$ and $\text{In}_{0.5225}\text{Al}_{0.4775}\text{As}$ for the wells and barriers, respectively, with the corresponding $\Delta E_c = 520$ meV.

The design constraints for both the strained and unstrained laser designs are (1) that the energy separation $\Delta_u = E'_u - E_u$ is ~ 60 meV and (2) that the energy separation Δ between the lower laser level and the ground state of the next downstream injector (i.e., the “reservoir” energy) is ~ 140 meV at the field at which the ground injector level and the upper laser level come into resonance. The same design philosophy was followed for both the unstrained and the strained laser designs. The injection barrier separating a given injector section from the following (downstream) active section was chosen to give a width of ~ 4 meV for the anticrossing between the injector ground level and the upper laser level, and the exit barrier separating a given active section from the following (downstream) injector section was chosen to give a width of ~ 6 meV for the anticrossing between the active ground level and the closest (in energy) level of the next downstream injector. The corresponding tunneling lifetimes (given by $\tau_{t,i} = h/2\Delta_i$, where Δ_i are the anticrossing widths) are 0.52 and 0.35 ps, respectively.

In the simplest approximation, the QC laser’s gain is proportional to the quantity:

$$R = \langle z \rangle^2 \tau_u (1 - \tau_l / \tau_{u \rightarrow l}), \quad (1)$$

where $\langle z \rangle$ is the optical matrix element for the transition between the upper (u) and lower (l) levels, τ_j is the lifetime of level j [$= u$ (for upper) or l (for lower)], and $\tau_{u \rightarrow l}$ is the inverse of the scattering rate between the upper and lower laser levels. It is assumed in calculating these quantities that the dominant scattering mechanism is LO (longitudinal optical) phonon scattering. The centers of the injector sections in each of the QC laser designs are doped to a level such that the average (3-D) dopant concentration of the active region is $2.2 \times 10^{16} \text{ cm}^{-3}$. Table 1 provides a summary of the critical design parameters pertinent to each of the three designs. As we can see from the table, the design parameters for the strained and unstrained designs are very similar, with the exception of the value of ΔE_c .

3 Laser Growth and Fabrication

We used conventional solid-source molecular-beam epitaxy (MBE) to grow the active regions of each of the strained and unstrained QC lasers on low-doped, n-type InP substrates. On either side of each active region, we grew 3500-Å-thick separate confinement (SC) layers comprised of lattice-matched (In,Ga)As to increase the optical confinement factor of the QC laser waveguide. The MBE-grown active regions were characterized using high-resolution x-ray diffraction (XRD). Figure 2 shows the XRD spectrum ([004] reflection) for wafer M738, the strained-active-region design. The spectrum shows the expected sequence of satellite peaks corresponding to the periodicity of the active region; from the peak separations, we extracted an active-region period that is only 0.8% larger than the design period, 603.3 Å. Furthermore, comparison of the measured spectrum with a dynamical simulation shows that the separation between the central satellite peak and the peak corresponding to the InP substrate is only 19.4 arcsec. Perfect lattice matching is achieved when the

Table 1 Key design parameters for the unstrained and strained QC laser designs.

Quantity	Description	M731 (unstrained)	M733 (unstrained)	M738 (strained)
x	In mole fraction in (In,Ga)As	0.5319	0.5319	0.5734
y	In mole fraction in (In,Al)As	0.5225	0.5225	0.4476
ε_x	Strain in (In,Ga)As	0	0	-0.00286
ε_y	Strain in (In,Al)As	0	0	0.00509
ΔE_c (meV)	Conduction-band offset	520	520	654.8
Δu (meV)	Energy separation between upper laser level and next higher energy active level	60.4	60.6	60.1
$\langle z \rangle_{ul}$ (\AA)	Optical matrix element	24.03	23.62	24.29
τ_u (ps)	Upper laser level lifetime	0.914	0.932	0.909
τ_l (ps)	Lower laser level lifetime	0.0999	0.1005	0.0997
$\tau_{u \rightarrow l}$ (ps)	Inverse of phonon scattering rate from level u to level l	2.565	2.627	2.510
N_{2D} (cm^{-2})	Sheet dopant concentration per period	1.30×10^{11}	1.30×10^{11}	1.33×10^{11}
n_{3D} (cm^{-3})	Average active-region dopant concentration	2.20×10^{16}	2.20×10^{16}	2.20×10^{16}

free-standing in-plane lattice constant of the strained structure, given by

$$a_{\text{par}} = \frac{\sum_j [G^{(j)} L^{(j)}]}{\sum_j [G^{(j)} L^{(j)} / a_0^{(j)}]}, \quad (2)$$

is equal to the InP substrate's lattice constant. In Eq. (2) $G^{(j)}$, $L^{(j)}$, and $a_0^{(j)}$ are, respectively, the shear modulus, the thickness, and the unstrained lattice constant of layer j , and the sum extends over all the layers within a single period of

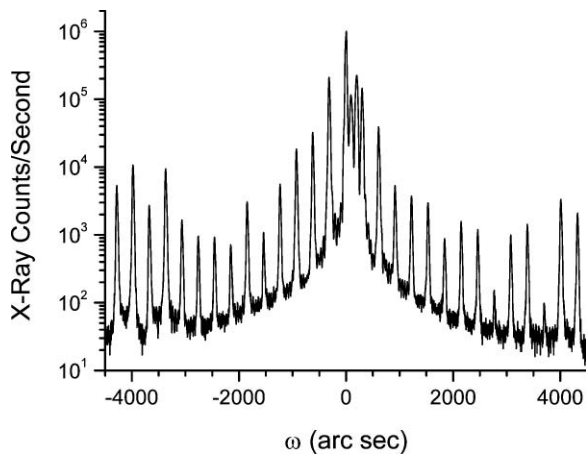


Fig. 2 XRD spectrum ([004] reflection) of wafer M738 with strain-balanced active region. The active-region period extracted from the XRD measurements is only 0.8% larger than the design value of the period, and the angular separation between the zero-order peak corresponding to the active region and the substrate peak is -19.4 arcsec.

the active region. According to Eq. (2), the predicted separation for the present perfectly strain-balanced structure between the central satellite peak and the InP substrate peak is 58.8 arcsec.

Similarly encouraging XRD results were obtained for the two unstrained active-region designs, verifying that the design values of the active periods (589.3 and 590.2 \AA , for M731 and M733, respectively) were reproduced within an error of <2% and that both structures were properly lattice matched to their InP substrates. Following XRD characterization of the MBE-grown active regions, we sent the wafers to an external vendor for growth of the lasers' InP top cladding and plasma confinement layers.

Double-channel ridge lasers were fabricated from the grown material using dry etching to form the laser ridges with vertical sidewalls. After etching the channels on either side of the ridge, we deposited a Si_3N_4 insulating dielectric layer over the entire surface using plasma-enhanced chemical vapor deposition (PECVD). Then a window was opened in the dielectric at the top of the ridge and a sequence of metal layers forming the ohmic contact to the semiconductor structure was deposited. Next, a two-step electroplating process was used to deposit a planarized gold blanket over the entire structure for improved thermal management. The thickness of the electroplated gold above the top of the ridge is $\sim 4 \mu\text{m}$. The wafer substrate was then lapped and polished, and a backside metallization sequence was deposited and annealed to reduce contact resistance. Finally, individual laser bars were cleaved from the processed material, and the rear facet on each of the bars was coated with a HR coating.

Individual lasers were diced from the cleaved and coated laser bars and mounted epi-side down onto AlN submounts

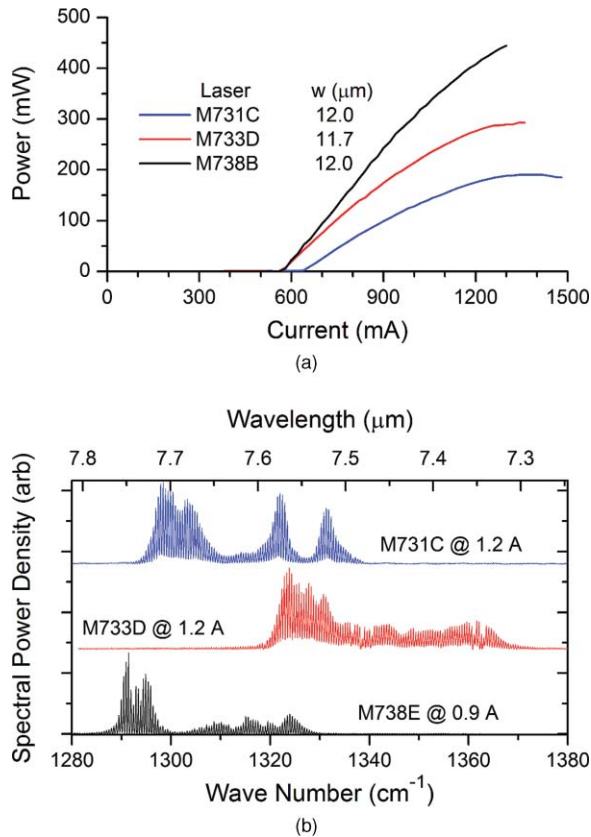


Fig. 3 (a) Output power as a function of current for lasers with similar ridge widths and 3-mm cavity lengths from each of the wafers under cw conditions. The heat-sink temperature is 25°C. All of the lasers have HR-coated rear facets. The laser (M738B) with the strained active region produces considerably more power than the other two. (b) Spectra (offset vertically for clarity) measured under the same conditions as in (a) at the indicated current values.

using AuSn solder. Laser/submount assemblies with 3-mm cavity lengths and with several different values of ridge width from each of the wafers were then mounted onto Cu blocks and wire bonded for testing.

4 Results of Laser Testing

The fabricated and mounted lasers were tested in cw mode near room temperature; for some of the lasers, we also measured the light-output-current-voltage (L - I - V) characteristics under short-pulse conditions (200 ns pulse width, 100 kHz pulse repetition rate, 2% duty cycle) at several temperatures to determine T_0 . Laser spectra were recorded in both cw and pulsed modes using a Fourier transform infrared spectrometer.

Figure 3(a) shows the measured cw light-output/current (L - I) characteristics for typical lasers with cavity lengths of 3 mm and ridge widths of $\sim 12 \mu\text{m}$ from each of the three wafers at a temperature of 25°C. Laser M738B, with a strained active region, produced a maximum of 444 mW of cw optical power at this temperature, whereas the two unstrained lasers, M731C and M733D, produced only 190 and 293 mW, respectively. The measured values of J_{th} and power slope efficiency S for each of the three lasers are, respectively, 1.77 kA/cm^2 and 0.388 W/A for M731C, 1.61 kA/cm^2 and 0.564 W/A for M733D, and 1.59 kA/cm^2

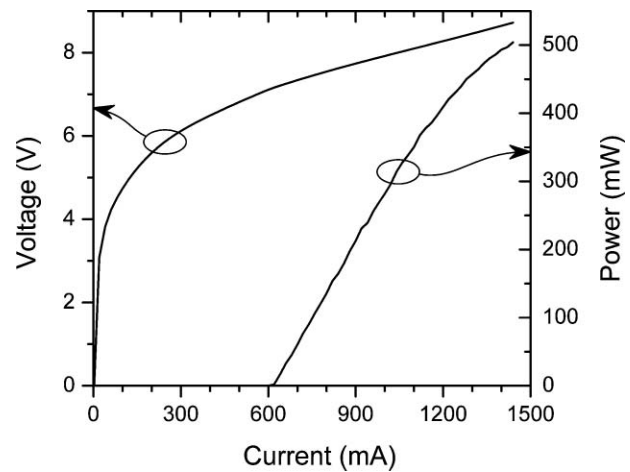


Fig. 4 Continuous-wave L - I - V characteristics of laser M738E, with a ridge width of 13.0 μm and a cavity length of 3 mm, at 25°C. Over 500 mW of optical power is produced.

and 0.738 W/A for M738B. Especially with respect to the values of S , the laser with the strained active region, M738B, is clearly superior to the other two. Figure 3(b) shows the measured multimode spectra of the three lasers, indicating that the emission wavelengths corresponding to M731 and M738 are in roughly the same spectral region, whereas M733 emits at somewhat shorter wavelengths (shifted from the M731 operating wavelength band by $\sim 0.15 \mu\text{m}$, as intended).

Another laser from wafer M738, with a 3-mm cavity length and a 13.0- μm ridge width, produced over 500 mW of cw optical power at 25°C (see Fig. 4). For this laser, the cw value of J_{th} is 1.59 kA/cm^2 , and the corresponding value of S is 0.757 W/A. To our knowledge, the results from this laser represent the highest cw output power obtained from any QC laser in the 7- to 8- μm spectral region that has been reported to date.

Figure 5 shows the measured cw values of J_{th} plotted as a function of ridge width for lasers from all three wafers at temperatures of 15 and 25°C. Some of the lasers failed during testing, and therefore not all the lasers shown at 25°C were able to be tested at 15°C, and vice versa. Nevertheless, the results obtained at the two temperatures appear to be consistent. They show that (1) the values of J_{th} over the entire range of ridge widths for lasers fabricated from wafer M731 are consistently larger by a significant amount than those fabricated from either wafer M733 or M738; (2) the ridge-width dependence of J_{th} for wafer M731, which covers a large range of ridge widths, is fairly weak, and it can be safely assumed that the ridge-width dependences of the other wafers are similar; (3) the values of J_{th} for wafer M738 lies somewhat below those of wafer M733. Figure 6 shows a plot of S extracted from cw L - I measurements as a function of ridge width for the same set of lasers as in Fig. 5 and at the same two temperatures. Here, we see that the S values for lasers fabricated from wafer M738 are clearly superior to the values for lasers fabricated from the other two wafers. It is still not well understood why the behaviors of lasers from the two wafers with unstrained active regions, M731 and M733, are different from one another; yet it is clear from all the data presented that the strained QC laser design, M738, is clearly superior to the two unstrained designs.

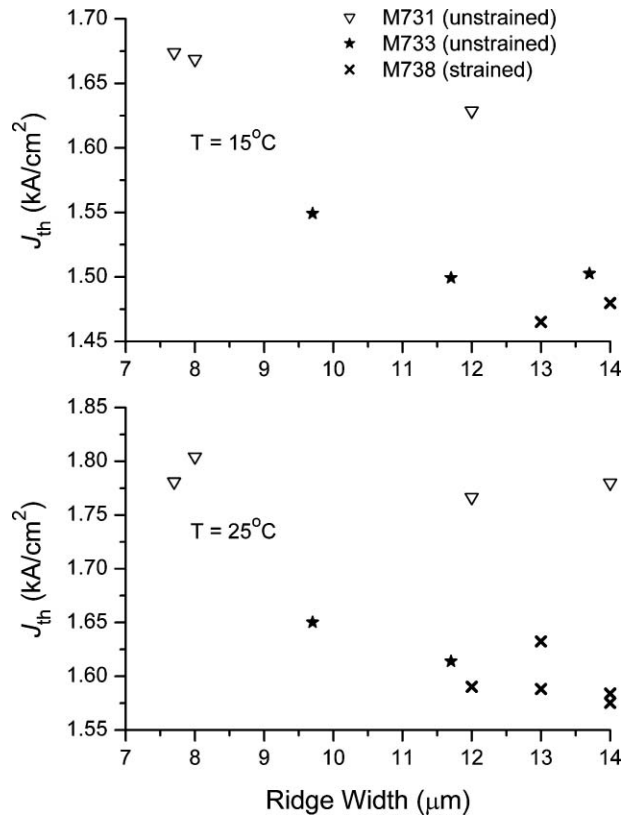


Fig. 5 Measured cw threshold current densities for different lasers fabricated from wafers M731, M733, and M738 as functions of laser ridge width at temperatures of 15 (top) and 25°C (bottom).

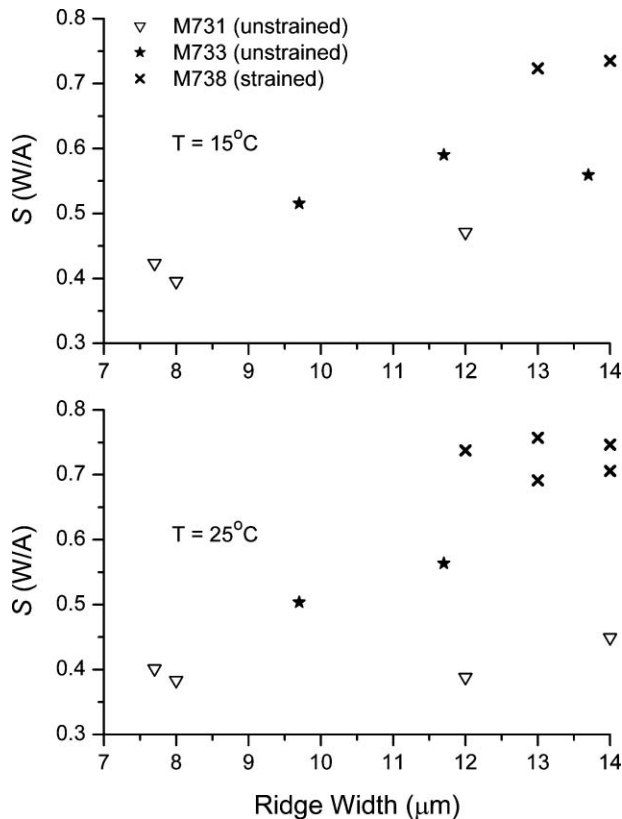


Fig. 6 Measured cw power slope efficiencies for different lasers fabricated from wafers M731, M733, and M738 as functions of laser ridge width at temperatures of 15 (top) and 25°C (bottom).

The weak dependences of threshold current density and slope efficiency on ridge width illustrated in Figs. 5 and 6 are consistent with the waveguide properties of our dry-etched laser ridges with vertical sidewalls. To show this, we modeled the 2-D ridge waveguide structure corresponding to M738 using the COMSOL multiphysics modeling software.¹⁴ The waveguide model includes both the Si_3N_4 dielectric and Ti-Au metallization layers along the ridge sidewalls, with the Ti layer included explicitly and the Au layer modeled as a nearly perfect metal. We calculated the laser waveguide modal refractive index, modal absorption coefficient, and optical confinement factor for the lowest order TM mode as a function of ridge width using material parameters that are appropriate for the M738 design already described, and for comparison we also calculated the same quantities for a 1-D (slab) waveguide corresponding to the same design. The waveguide quantities of interest in analyzing the results of Figs. 5 and 6 are easily determined from the fundamental expressions for the transparency current density and power slope efficiency, which are as follows, respectively.⁵

$$J_{th} = J_{tr} + (\alpha_m + \alpha_w)/(g\Gamma), \quad (3)$$

$$S = \frac{hc\eta_i}{\lambda} \frac{\alpha_m}{\alpha_m + \alpha_w}. \quad (4)$$

In Eqs. (3) and (4), J_{tr} is the transparency current density, α_m is the mirror loss, α_w is the waveguide loss, g is the material differential gain, Γ is the waveguide mode's optical confinement factor, h is Planck's constant, c is the speed of light, η_i is the internal quantum efficiency of the laser, and λ is the laser wavelength.

Guided by the dependences of J_{th} and S on waveguide-related properties in Eqs. (3) and (4), Fig. 7 shows the results of the COMSOL calculation, where we have plotted as functions of ridge width the calculated values of $(\alpha_m + \alpha_w)/\Gamma$ on the left axis and $\alpha_m/(\alpha_m + \alpha_w)$ on the right axis, where in both cases we normalized the results to the respective values

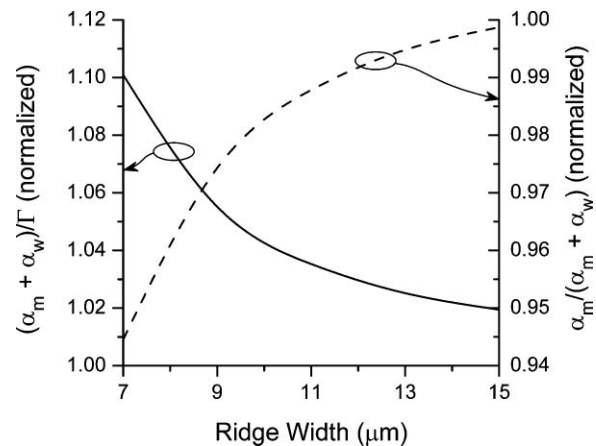


Fig. 7 Results of simulating the ridge-width dependences of the waveguide properties of the strained QC laser design, M738, using a 2-D implementation of the COMSOL software. Left axis and solid curve: ratio of total loss (waveguide plus mirror) to the modal confinement factor, normalized to the value obtained in a 1-D (slab) calculation. Right axis and dashed line: ratio of mirror loss to total loss, again normalized to the value obtained in a slab calculation. The calculations are in accord with experimental results showing only a small variation of measured laser threshold current density and power slope efficiency with ridge width.

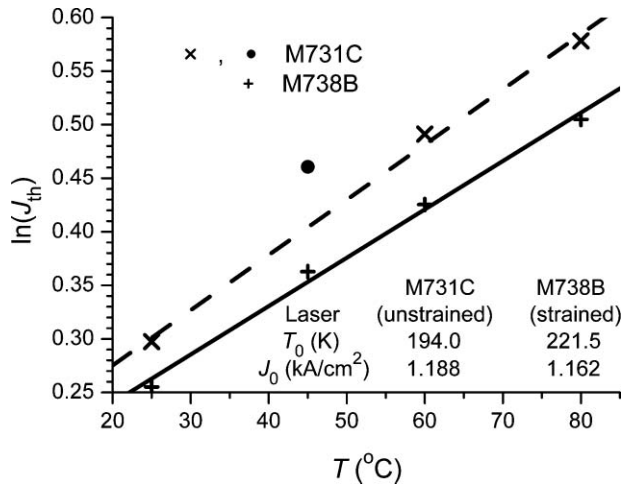


Fig. 8 Results of fitting the logarithm of J_{th} as a function of temperature for pulsed (200 ns pulse width, 100 kHz pulse repetition rate, 2% duty cycle) operation of lasers M731C (unstrained) and M738B (strained) as functions of temperature. Both lasers have 12- μm ridge widths and 3-mm cavity lengths. Values of T_0 and J_0 extracted from the fits are shown. The data point at $T = 45^\circ\text{C}$ for M731, represented by the circle, was excluded from the fit on statistical grounds.

obtained for the slab waveguide. The results clearly show the weak dependence of these quantities on ridge width, with the calculated values varying by only ~ 8 and $\sim 5.5\%$, respectively, for ridge widths between 7 and 15 μm . Our waveguide modeling studies also show that this variation is considerably lower than that for waveguides with sloping sidewalls (e.g., those obtained in wet-etching processes). This is because the electric field in the calculated TM mode for the vertical-sidewall structure has a negligible tangential component at the sidewall interfaces, even in the absence of the metal, and therefore the sidewall absorption in structures with vertical sidewalls is lower than in structures with sloping sidewalls.

We also measured the threshold currents of the lasers with 12- μm ridge widths from the strained design (laser M738B) and from one of the unstrained designs (M731C) as a function of temperature under pulsed conditions (200 ns pulse width, 100 kHz pulse repetition rate, 2% duty cycle) to determine T_0 , which is defined through the relationship

$$J_{\text{th}}(T) = J_0 \exp(T/T_0), \quad (5)$$

where T is the active-region temperature in degrees Celsius and where J_0 is a constant, equal to the value of J_{th} at $T = 0^\circ\text{C}$. The negligible heating under the low-duty-cycle pulsed operating conditions used for the measurements enables us to ignore any temperature differences between the active-region and heat-sink temperatures. The measurements were made over the temperature range between 25 and 80°C , and values of T_0 and J_0 were determined for each set of measurements by performing a linear least-squares fit to $\ln(J_{\text{th}})$ as a function of temperature. The results are indicated in Fig. 8. For M731, we excluded the data point at $T = 45^\circ\text{C}$ (represented by a circle in Fig. 8) from the fit because this data point lies more than three standard deviations away from the straight-line fit. The values of T_0 extracted from the data are 221.5 ± 12.6 K for M738B and 194.0 ± 11.7 K for M731C. To our knowledge, the former T_0 value is the largest

ever measured above room temperature for QC lasers in this wavelength range.

5 Discussion and Conclusions

In summary, we designed, grew, and fabricated QC lasers with strain-balanced active regions in the 7.3- to 7.8- μm wavelength region and compared their performance with that of unstrained QC lasers with the same emission wavelengths. One of the strained QC lasers produced more than 500 mW of cw, room-temperature output power. The characteristic temperature for this laser design under pulsed operation was determined as $T_0 = 221.5 \pm 12.6$ K between 25 and 80°C . To our knowledge, this is the largest T_0 value ever measured above room temperature for QC lasers in this wavelength range.

The question naturally arises whether the observed improvements result from changes in the electronic structure associated with the increased conduction-band offset in the strained material system or whether, for example, the use of the strained-layer material system results in improved MBE material growth, particularly improved interfaces between the layers comprising the laser's active region. As indirect evidence of the former, we can cite several factors. First, we would expect improved growth interfaces to result in reduced interface roughness scattering,¹⁵ leading to a reduction in the linewidth of the laser transition and therefore an enhancement in the gain peak, whose primary effect on the presented results would have been lowered threshold current density but not a large improvement in slope efficiency as was observed. Second, the results obtained from the T_0 analysis suggest that high-temperature mechanisms influence the threshold; to the degree that the results in Fig. 8 can be extrapolated to lower temperatures, the two fit curves should merge at $T \sim -35^\circ\text{C}$. If our results were due to improved MBE growth of strained structures, one would expect that the performance improvement in the strained M738 design would persist to much lower temperatures. Finally, the nature of the electronic structures of the strained and unstrained designs themselves suggests improved performance for the former: excited downstream injector levels (such as those depicted by the light green and blue lines in Fig. 1) are positioned in a similar manner relative to the upper laser level in both the strained and unstrained designs; however, the pathway to the continuum from these levels in the former case involves a much greater energy barrier than in the latter. In fact, in comparison with the energy of the barrier's band edge at the center of an injector region, the energy of the lowest excited injector level is ~ 110 meV below this barrier energy in the strained design but ~ 45 meV above the barrier energy in the unstrained designs! These factors suggest that the differing band offsets in the strained versus the unstrained designs play a significant role in explaining the performance difference; however, further study, including measurements conducted over a range of temperatures between cryogenic and room temperatures, would be expected to more clearly elucidate these issues.

Acknowledgments

A portion of the work reported here was conducted under a Cooperative Research and Development Agreement with the Army Research Laboratory, Agreement No. 0905-A-C117.

References

1. J. Faist, F. Capasso, D. L. Sivco, C. Sirtori, A. L. Hutchinson, and A. Y. Cho, "Quantum cascade laser," *Science* **264**(5158), 553–556 (1994).
 2. M. Beck, D. Hofstetter, T. Aellen, J. Faist, U. Oesterle, M. Ilegems, E. Gini, and H. Melchior, "Continuous-wave operation of a mid-infrared semiconductor laser at room temperature," *Science* **295**(5553), 301–305 (2002).
 3. R. Maulini, S. Yarekha, J. M. Bulliard, M. Giovannini, and J. Faist, "Continuous-wave operation of a broadly tunable thermoelectrically cooled external cavity quantum cascade laser," *Opt. Lett.* **30**(19), 2584–2586 (2005).
 4. J. S. Yu, S. Slivken, S. R. Darvish, A. Evans, G. Gokden, and M. Razeghi, "High-power, room-temperature, and continuous-wave operation of distributed-feedback quantum-cascade lasers at $\lambda \sim 4.8 \mu\text{m}$," *Appl. Phys. Lett.* **87**, 041104-1–041104-3 (2005).
 5. J. S. Yu, S. Slivken, A. J. Evans, and M. Razeghi, "High-performance, continuous-wave operation of $\lambda \sim 4.6 \mu\text{m}$ quantum-cascade lasers above room temperature," *IEEE J. Quantum Electron.* **44**(8), 747–754 (2008).
 6. Y. Bai, S. Slivken, S. R. Darvish, and M. Razeghi, "Room temperature continuous wave operation of quantum cascade lasers with 12.5% wall plug efficiency," *Appl. Phys. Lett.* **93**, 021103-1–021103-3 (2008).
 7. A. Lyakh, R. Maulini, A. Tsekoun, R. Go, C. Pflügl, L. Diehl, Q. J. Wang, F. Capasso, and C. K. N. Patel, "3 W continuous-wave room temperature single-facet emission from quantum cascade lasers based on nonresonant extraction design approach," *Appl. Phys. Lett.* **95**, 141113-1–141113-3 (2009).
 8. M. Razeghi, Y. Bai, S. Slivken, S. Kuboya, and S. R. Darvish, "Recent performance records for mid-IR quantum cascade lasers," in *Proc. Int. Workshop on Terahertz and Mid-Infrared Radiation: Basic Research and Practical Applications*, ITAP, Turunç-Marmaris, Turkey (2009), pp. 3–4.
 9. A. Evans, J. S. Yu, J. David, L. Doris, K. Mi, S. Slivken, and M. Razeghi, "High-temperature, high-power, continuous-wave operation of buried heterostructure quantum-cascade lasers," *Appl. Phys. Lett.* **84**(3), 314–316 (2004).
 10. L. Diehl, D. Bour, S. Corzine, J. Zhu, G. Höfler, M. Loncar, M. Troccoli, and F. Capasso, "High-power quantum cascade lasers grown by low-pressure metal organic vapor-phase epitaxy operating in continuous wave above 400 K," *Appl. Phys. Lett.* **88**, 201115-1–201115-3 (2006).
 11. C. Pflügl, L. Diehl, A. Tsekoun, R. Go, C.K.N. Patel, X. Wang, J. Fan, T. Tanbun-Ek, and F. Capasso, "Room-temperature continuous-wave operation of long wavelength ($\lambda = 9.5 \mu\text{m}$) MOVPE-grown quantum cascade lasers," *Electron. Lett.* **43**(19), 1026–1028 (2007).
 12. J. S. Yu, S. Slivken, A. Evans, S. R. Darvish, J. Nguyen, and M. Razeghi, "High-performance, continuous-wave quantum-cascade lasers operating up to 85°C at $\lambda \sim 8.8 \mu\text{m}$," *Appl. Phys. A* **93**, 405–408 (2008).
 13. M. Razeghi, S. Slivken, Y. Bai, B. Gokden, and S. R. Darvish, "High power quantum cascade lasers," *New J. Phys.* **11**, 125017 (2009).
 14. <http://www.comsol.com>.
 15. J. B. Khurgin, Y. Dikmelik, P. Q. Liu, A. J. Hoffman, M. D. Escarra, K. J. Franz, and C. F. Gmachl, "Role of interface roughness in the transport and lasing characteristics of quantum-cascade lasers," *Appl. Phys. Lett.* **94**, 091101-1–091101-3 (2009).
- Richard P. Leavitt** received his BS degree in physics from Lowell Technological Institute in 1970 and his PhD degree in physics from the University of Lowell in 1976. He was at the U.S. Army's Harry Diamond Laboratory (now part of the Army Research Laboratory) from 1970 to 1974, from 1976 to 1985, and from 1989 to 2001. From 1974 to 1976 he was with Avco Everett Research Laboratory, and he was also with Martin Marietta Laboratory between 1985 and 1989. In 2001, he joined Quantum Photonics, Inc. (now Covega). Since 2003 he has been with Maxion Technologies, Inc., where he is responsible for the design of quantum and interband cascade lasers and type-II superlattice IR detectors. He has over 140 refereed publications in scientific and technical journals, books, and conference proceedings. Dr. Leavitt's research interests are fundamental physics and device applications of semiconductor optoelectronic devices.
- John L. Bradshaw** received his BS and MS degrees in physics from Lehigh University in Bethlehem, Pennsylvania in 1982 and 1984, respectively, and his PhD degree in physics from the University of Pittsburgh, Pennsylvania, in 1989. He was a National Research Council postdoctoral associate at the U.S. Army Harry Diamond Laboratories, Adelphi, Maryland, from 1989 to 1991, and a member of the technical staff of the Army Research Laboratory (ARL) from 1991 to 2001. In 2001, Dr. Bradshaw cofounded Maxion Technologies, Inc., which was acquired by Physical Sciences, Inc., of Andover, Massachusetts, in September 2009. Dr. Bradshaw is currently a senior principal scientist at Maxion, concentrating on measurements and applications of quantum cascade and interband cascade lasers for government, commercial, and military uses. Dr. Bradshaw is a member of the SPIE.
- Kevin M. Lascola** received his BS degree in electrical engineering from the University of Maryland, College Park, in 1995, and his MS degree in electrical engineering from the University of California, Berkeley, in 1997. From 1997 to 2006, Mr. Lascola was a product engineer and engineering manager at SDL and JDS Uniphase with engineering responsibility for GaAs- and InP-based lasers for telecommunications as well as for high-speed *p-i-n* and avalanche photodiode (APD) photodetectors. From 2006 to 2007, Mr. Lascola was a senior product engineer for Fusion UV Systems, where he worked on various microwave-powered UV light sources. In 2007, Mr. Lascola joined Maxion Technologies, where he is currently a principal scientist with responsibility for the engineering and fabrication of quantum cascade and interband cascade lasers.
- Gregory P. Meissner** is currently with General Technical Services, LLC, and works at the Army Research Laboratory. His biography is unavailable.
- Frankie Micalizzi** is currently employed by Sigma Space Corporation and works at the National Aeronautics and Space Administration (NASA) Goddard Space Flight Center. His biography is unavailable.
- Frederick J. Towner** received his BS degree in physics from Penn State University in 1986 and his MS degree in electrical engineering from the University of Maryland, Baltimore County, in 1992. From 1986 to 1995, he was with Martin Marietta Laboratories in Catonsville, Maryland, where he performed molecular-beam epitaxy (MBE) crystal growth and materials characterization for R&D programs in 980-nm lasers, quantum-well IR photodetectors, electro-optic modulators, and millimeter-wave ICs. In 1995, he joined the University of Maryland's Laboratory for Physical Sciences, performing MBE growth and materials characterization of a variety of electro-optic devices. In 1997, he joined Quantum Epitaxial Designs, a commercial MBE epi vendor, as a senior production engineer, eventually becoming production engineering manager. In 2002, Mr. Towner joined Maxion Technologies, where he has been responsible for Maxion's crystal growth and material characterization. Mr. Towner currently has over 35 journal publications.
- John T. Pham** received his BS degree in electrical engineering from the University of Maryland, College Park, in 1989. He was an electronics engineer at the Army Research Laboratory, Adelphi, Maryland, from 1989 to 2001. In 2001, Mr. Pham cofounded Maxion Technologies, Inc., which was acquired by Physical Sciences, Inc., of Andover, Massachusetts, in September 2009. Mr. Pham is currently a senior engineer at Maxion, working on fabrication development of quantum and interband cascade lasers for government, commercial, and military uses.

Photographs of authors are not available.